



## Effect of heat treatments on microstructural and mechanical characteristics of dissimilar friction stir welded 2198/2024 aluminum alloys

Mahdi Masoumi Khalilabad, Yasser Zedan, Damien Texier, Mohammad Jahazi & Philippe Bocher

To cite this article: Mahdi Masoumi Khalilabad, Yasser Zedan, Damien Texier, Mohammad Jahazi & Philippe Bocher (2021): Effect of heat treatments on microstructural and mechanical characteristics of dissimilar friction stir welded 2198/2024 aluminum alloys, Journal of Adhesion Science and Technology, DOI: [10.1080/01694243.2021.1917868](https://doi.org/10.1080/01694243.2021.1917868)

To link to this article: <https://doi.org/10.1080/01694243.2021.1917868>



© 2021 The Author(s). Published by Informa UK Limited, trading as Taylor & Francis Group.



Published online: 03 May 2021.



[Submit your article to this journal](#)



Article views: 480



[View related articles](#)



[View Crossmark data](#)



Citing articles: 1 [View citing articles](#)

# Effect of heat treatments on microstructural and mechanical characteristics of dissimilar friction stir welded 2198/2024 aluminum alloys

Mahdi Masoumi Khalilabad<sup>a</sup>, Yasser Zedan<sup>b</sup>, Damien Texier<sup>b,c</sup>, Mohammad Jahazi<sup>b</sup> and Philippe Bocher<sup>b</sup>

<sup>a</sup>Faculty of Engineering Technology, University of Twente, Enschede, The Netherlands; <sup>b</sup>Mechanical Engineering Department, École de Technologie Supérieure (ÉTS), Montreal, Canada; <sup>c</sup>Clement Ader Institute (ICA), University of Toulouse, Toulouse, France

## ABSTRACT

The 3<sup>rd</sup> generation of aluminum–lithium (Al–Li) alloys provides a desirable combination of high mechanical properties and low density compared to their traditional counterparts, exempt of lithium. Therefore, providing a reliable joint between new and conventional aluminum alloys is crucial for making hybrid structures. The present study focuses on improving the mechanical properties of dissimilar AA2198/AA2024 joints using different heat treatments before and after welding. Tensile tests paired with digital image correlation (DIC) techniques and micro-hardness maps were performed to document the macro-scale and local mechanical behavior of the joints. As-welded joints demonstrated a similar yield strength, 30% lower than that of the base metals in T3 and T8 metallurgical states. As-welded joints failed at the AA2198 side in the heat affected zone (HAZ), parallel to the thermo-mechanically affected zone (TMAZ), region experiencing intense strain concentration and minimal hardness values. Post welding-heat treatments (PWHT) was found to successfully strengthen HAZ on the AA2198 side, without abnormal grain growth in the nugget and impairing the hardness properties on AA2024 side. This improvement in local mechanical properties on the AA2198 side was related to the re-precipitation of dissolved T1 (Al<sub>2</sub>CuLi) and  $\theta$  (Al<sub>2</sub>Cu) during welding as characterized by differential scanning calorimetry (DSC) and microscopy analyses. However, PWHT joint variants demonstrated a reduction in total elongation and ultimate tensile strength due to intense strain localization on the AA2024 retreating side compared to a much more homogeneous strain distribution in the as-welded joints.

## ARTICLE HISTORY

Received 28 December 2020  
Revised 7 April 2021  
Accepted 11 April 2021

## KEYWORDS

Friction stir welding; heat treatment; digital image correlation (DIC); differential scanning calorimetry (DSC); aluminum–lithium (Al–Li) alloys

## 1. Introduction

The 3<sup>rd</sup> generation of aluminum–lithium (Al–Li) alloys is ideal for the transport industry when weight reduction is a priority. However, the main drawback of Al–Li alloys is

**CONTACT** Mahdi Masoumi Khalilabad  [m.masoumikhililabad@utwente.nl](mailto:m.masoumikhililabad@utwente.nl)  Faculty of Engineering Technology, University of Twente, Enschede, The Netherlands

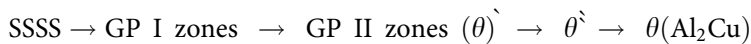
© 2021 The Author(s). Published by Informa UK Limited, trading as Taylor & Francis Group.

This is an Open Access article distributed under the terms of the Creative Commons Attribution License (<http://creativecommons.org/licenses/by/4.0/>), which permits unrestricted use, distribution, and reproduction in any medium, provided the original work is properly cited.

their complex manufacturing process, making them particularly expensive compared to conventional aluminum alloys. A cost- and weight-efficient solution for aerospace structures consists of using Al–Li alloys only for critical regions, while the rest of the structure being made of conventional aluminum alloys. Dissimilar joining of conventional aluminum alloys to Al–Li alloys appears as a vital solution for design-efficient structures.

The conventional fusion welding methods are inappropriate for joining the 3<sup>rd</sup> generation Al–Li alloys due to welding defects, for example, hot cracking [1,2]. The friction stir welding (FSW) process, a solid-state welding technique, prevents the formation of such detrimental welding defects [3,4]. However, even the solid-state FSW process generally produces a significant heat input, leading to potential microstructural changes. Indeed, over-aging or strengthening precipitates dissolution within the nugget zone (NZ), the thermo-mechanically affected zone (TMAZ), or the heat-affected zone (HAZ) of FSWed joints was reported to occur [5,6].

Loss of mechanical properties is generally observed in these microstructure-evolving areas, especially at TMAZ and HAZ [7–9]. Thus, it is essential to understand the microstructural changes during the FSW process. Heidarzade et al. [10] have written an excellent review on FSW processes of dissimilar materials and their microstructural evolutions. They have addressed challenges associated with joining a broad range of dissimilar material combinations. In their work, the precipitation sequence of binary Al–Cu alloys from the supersaturated solid solution (SSSS) was reported as follow:



However, the precipitation sequence in Al–Li alloys is more complex. The 3<sup>rd</sup> generation alloys have a lower Li content compared to the 1<sup>st</sup> and 2<sup>nd</sup> generations of Al–Li alloys, thus avoiding the formation of brittle  $\delta^I(\text{Al}_3\text{Li})$  phases and improving toughness properties. Besides, higher Cu and Mg amounts promote the formation of T1 ( $\text{Al}_2\text{CuLi}$ ) strengthening phases [11]. In the specific case of similar joints made of only AA2198 material, a drop of strength properties was reported, resulting from the dissolution of T1 ( $\text{Al}_2\text{CuLi}$ ) precipitates at high welding temperatures [12]. Similarly, joints made of AA2024 have a lower hardness at HAZ and TMAZ [13]. Despite intense optimization in welding parameters and cooling during the welding operation, the mechanical performance of FSWed joints is always lower than those of both the base metals [14–16]. Therefore, the dissimilar welding of AA2024 and AA2198 is particularly challenging owing to the local evolution of the microstructure and mechanical properties due to severe thermomechanical stress inherent to the FSW process.

The post-weld heat treatment (PWHT) has been targeted in the present research to improve the joint mechanical properties. PWHT can be a combination of solution heat treatment and aging treatment or merely an aging treatment after welding [17]. Applying bulk or local PWHT on AA2××× series leads to a fine and dense re-precipitation in the NZ [18], resulting in recovering the joint mechanical properties [19–21]. Lin. et al. [22] investigated the influences of PWHT on the microstructure and tensile properties of Al–Cu–Li alloys. A significant improvement in tensile strength and hardness properties of the joint was reported by applying pre-straining then aging

**Table 1.** Chemical compositions of base materials AA2024 and AA2198 (wt.%).

Material	Cu	Li	Mg	Ag	Mn	Fe	Zn	Si	Ti	Al
AA2024	3.7–4.8	-	1.1–1.7	-	0.2–0.8	≤0.5	0.2	≤0.5	0.15	Bal.
AA2198	2.9–3.5	0.8–1.1	0.3–0.8	0.1–0.5	≤0.5	≤0.01	≤0.36	≤0.08	-	Bal.

treatment on FSWed joints. However, the combination of solution and aging treatment resulted in the joint ductility impairment, which was correlated to coarse  $\delta^I$  ( $\text{Al}_3\text{Li}$ ) precipitates, producing high-stress concentration during plastic deformation. Moreover, Zhang et al.[23] reported that the combination of solution and aging treatment of Al–Li alloys could decrease the ductility due to grain coarsening in the NZ and TMAZ. Moradi et al. [21] investigated the effect of PWHT on microstructural and mechanical properties of dissimilar joints between AA2024 and AA6061. The aging treatments improved the joint efficiency up to 96% of base metal AA6061. However, remarkable abnormal grain growth in the nugget of joint was reported. Therefore, improving the joint performance with PWHT is not straightforward compared to similar joints and a closer investigation is needed.

Dissimilar FSWed joints made of AA2198 and AA2024 have already been investigated in terms of mechanical and microstructural characterizations [24–27]. To the authors' knowledge, neither pre- nor post-welding heat treatments were applied to dissimilar joints between AA2024 and AA2198 in the literature. Therefore, this research addresses the challenge of optimizing heat treatment for dissimilar joints made of AA2198 and AA2024, in order to improve the weakest as-FSWed regions without impairing the rest of the joint.

## 2. Experimental procedures

### 2.1. Base materials

Rolled sheets of AA2024 and AA2198 with a thickness of 3.2 mm, both in T3 heat treatment conditions, were used for the present investigation. The chemical composition of the base materials is reported in Table 1.

3D Optical micrographs of the grain structure for AA2024 and AA2198 in T3 heat treatment conditions can be seen in Figure 1(a,b), respectively. The grain structure of AA2024 is relatively equiaxed. However, AA2198 consists of an elongated grain structure. The microstructure of the base metals was detailed in Zhu et al. [28] and Lv et al. [29].

### 2.2. FSW process

Selecting the appropriate tool design is the first step for a successful FSW process. In this research, a tapered cylindrical pin with a fan shoulder was chosen as a suitable design to join AA2198 and AA2024 based on a recent investigation [27]. A rotation speed and a traverse speed of 750 rpm and  $50 \text{ mm min}^{-1}$  were used for the welding process. A quenched and tempered AISI 4340 steel with a hardness of 49 HRC was used as the FSW tool material. The shoulder diameter was 15.8 mm. The pin length and diameter were 2.7 and 4.7 mm, respectively. The tool geometry is depicted in

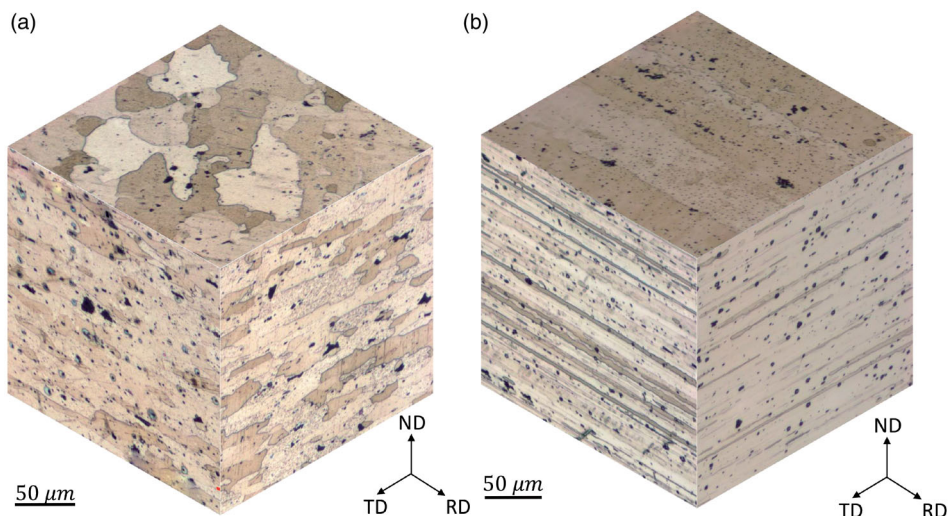


**Figure 1.** 3D optical micrographs of base materials grain structure in T3 heat treatment condition (a) AA2024 and (b) AA2198.

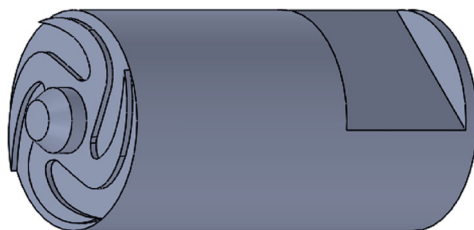


**Figure 2.** Tool configuration used for the FSW process. The tool is composed of a fan shoulder with a tapered cylindrical pin.

**Figure 2.** A specific fixture was manufactured to ensure the repeatability and reliability of the FSW process, as shown in **Figure 3**. The weld line was parallel to the AA2024 rolling direction (RD) and the AA2198 traverse direction (TD), as suggested in Robe et al. [24]. In this paper, the welding direction, the cross-weld direction, and the normal direction are indicated by WD, CWD, and ND, respectively.

The temperature during welding was measured at both the advancing side (AS) and the retreating side (RS). K-type thermocouples with a diameter of 1 mm were used to measure thermal profiles in the TMAZ and HAZ regions. The thermocouples were placed in drilled holes on the weld line and 2 mm away from the weld line. Thermigrease TG 20033 paste was used to protect them and improve thermal reactivity.

### 2.3. Pre-welding and post-welding heat treatments

The recommended temperature and time for T8 artificial aging of AA2024 are 463 K and 12 h, while they are 448 K and 14 h for AA2198 [30,31]. Based on trial heat treatment tests on both materials, 448 K and 12 h were found as the optimal aging treatment parameters.

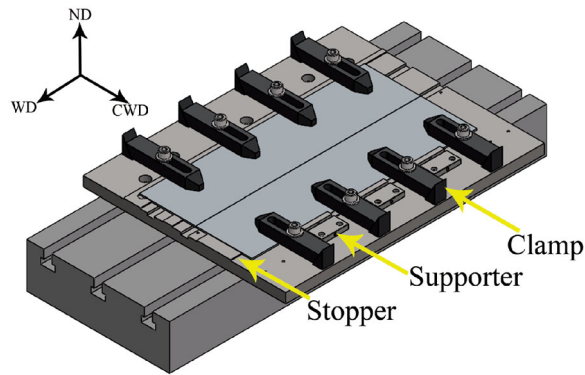


**Figure 3.** Schematic illustration of the manufactured fixture for the reliability and repeatability of the FSWed joints.

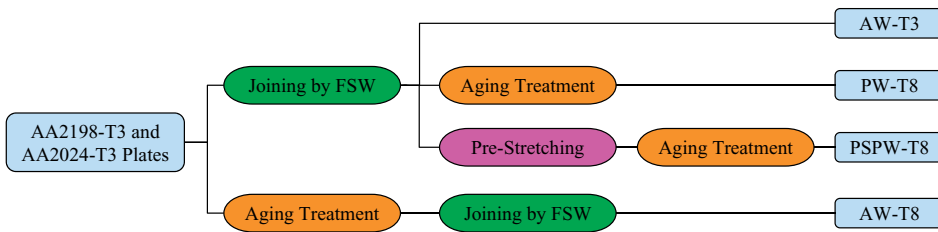


**Figure 4.** Procedure to elaborate FSWed samples and the associated categories. AW-T3 and AW-T8 are as-welded samples, while PW-T8 and PSPW-T8 are post-weld heat treated samples.

In order to investigate the effect of pre-welding heat treatment and post-welding thermomechanical treatments on the tensile performance of FSWed dissimilar joints of AA2198 and AA2024, four categories of samples were produced as shown in **Figure 4**: (i) T3 as-welded joints (AW-T3), (ii) T8 as-welded joints (AW-T8), (iii) T8 post-welding heat treatment (PW-T8), and (iv) 3% pre-stretching followed by T8 post-welding heat treatment (PSPW-T8). Both PWHT were applied to AW-T3 joints.

### 2.4. Microstructure characterization

The metallography and micro-hardness samples were polished according to the standard polishing procedure up to a 1  $\mu\text{m}$  size of diamond paste. The specimens were then mechano-chemically polished with a colloidal silica solution (0.05  $\mu\text{m}$ ) using a BUEHLER VibroMet polishing machine for 48 h. The joint microstructure was revealed using Keller’s reagent (2 mL HF, 3 mL HCl, 5 mL HNO<sub>3</sub>, 190 mL H<sub>2</sub>O) for 15 s. Laser scanning confocal microscope model OLYMPUS Lext OLS4100 was used to obtain the large optical micrographs through automated stitching operation. Field emission gun-scanning electron microscope (FEG-SEM), model HITHACHI SU8200, equipped with EDS, was used for precipitates characterization and fractography.

Differential scanning calorimetry (DSC) measurements were conducted with a PerkinElmer Simultaneous Thermal Analyzer (STA) 6000. The DSC analyses were

performed under nitrogen flux. DSC samples were discs with a diameter of 4 mm and a thickness of 0.5 mm. The samples were kept at an initial temperature of 323 K for 1 min to provide sufficient time for the thermal stabilization of the apparatus. DSC analyses were then conducted with a heating rate of  $10 \text{ K min}^{-1}$  from 323 to 823 K.

### **2.5. Mechanical testing for macroscopic and local characterizations**

Tensile test samples were machined from the base materials and joint variants by CNC machining. Tensile specimens were machined so that the loading direction was parallel to TD for base material AA2024, RD for AA2198, and CWD for welded samples. In order to remove the defects such as kissing bond or flash, both the sides of the tensile samples were polished.

A micro-tensile device model Kammrath & Weiss 5 kN was used for assessing the mechanical behavior of all the sample variants. A constant cross-head displacement rate of  $7 \mu\text{m s}^{-1}$ , that is, a strain rate of approximately  $2.3 \times 10^4 \text{ s}^{-1}$ , was selected for tensile tests. To assess the global tensile behavior of the joints, the sample deformation along the loading direction was continuously recorded with an optical extensometer (model Keyence LS-7030M), sampling the extremities of both the TMAZ locations ( $L_0 = 16 \text{ mm}$ ). Loading was applied along the cross-welding direction (CWD). The tensile tests were repeated three times to ensure the reliability of the results.

The optical high resolution-digital image correlation (OHR-DIC) technique was used to calculate the local strain fields within the joint area from full-field kinematics measurements. The technical details are available in Texier et al. [25]. The optical microscope model OLYMPUS DSX-500 was employed in a dark field mode. To track regions on the sample surface, the speckle pattern was carried out using Keller's etchant. An open-source DIC software developed at LOPFA (OpenDIC [32]) was used to assess the in-plane local displacement fields. Twelve regions of interest were required to capture the whole joint from one HAZ region to the other HAZ region. Calculation of the kinematic fields was conducted for each region of interest. Individual strain maps were subsequently stitched together to obtain the strain map of the whole joint. The strain fields were determined with a JAVA companion working with Fiji software.

The local heterogeneous mechanical behavior within the joints was also assessed by microhardness measurements. Vickers hardness maps were carried out using an automatic CLEMEX micro-hardness machine. The indentation load and time of 25 gf and 10 s were selected. Grids in the CWD-ND plane of  $31 \times 260$  measurements (in total 2480 indents) with a step size of  $80 \mu\text{m}$  were performed for all the FSWed sample variants to analyze the hardness distribution on the whole joint.

## **3. Results and discussion**

### **3.1. Microstructural characterization**

Macrographs were performed for pre and post-welding heat-treated joints. Similar FSW macrostructures were observed in all joint variants. Joints were exempt from defects. Figure 5 illustrates a typical FSW macrograph in the CWD-ND and CWD-WD planes of sample AW-T3. The transition between BM and HAZ is difficult to

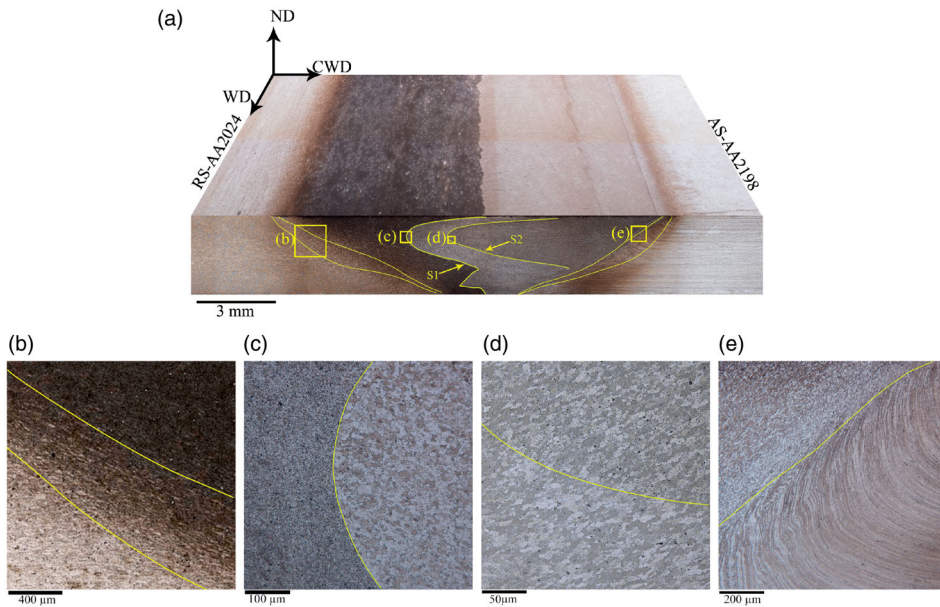


**Figure 5.** Typical microstructure of joint AW-T3 on CWD-ND cross-section, (a) joint macrograph, (b) retreating side transition, (c) S1 border inside joint, (d) S2 border inside joint, (e) advancing side transition.

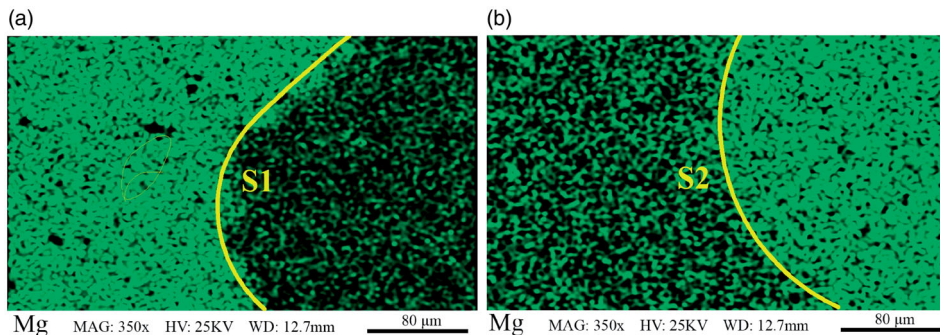


**Figure 6.** EDS map of Mg element in the joint region around (a) S1 border, and (b) S2 border.

determine in both advancing and retreating sides based on macrograph observations (Figure 5(a)). A thick and smooth transition band was found between the TMAZ and NZ on the AA2024-RS (Figure 5(b)). The nugget consisted of three zones separated by two S- shape borders (S1 and S2) due to the variant flow rate of material in the center and around of FSW pin. A very fine recrystallized microstructure was observed for the three zones, as shown in Figure 5(c) and d. S1 border separated both the materials AA2024 with very fine grains and AA2198 with fine grains, as shown in Figure 5(c). The S2 border divided the AA2198 material into two zones with no significant difference in terms of grain size (Figure 5(d)). However, the distribution of Mg elements on both sides of S1 and S2 borders is inequivalent, thus confirming the heterogeneous nature of the nugget region (Figure 6). A similar zone between S1 and S2 borders at the AA2024-AA7075 FSW joints interface was reported [10,33]. The origin of this

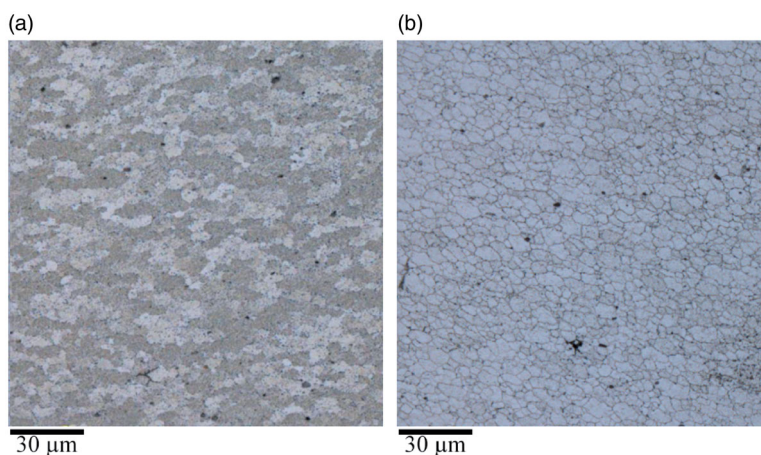


**Figure 7.** The effect of PWHT on grain size of nugget center. (a) AW-T3 grain structure, and (b) PSPW-T8 grain structure.

microstructural evolution is not clear yet. It may be related to different recrystallization mechanisms, and it requires more texture investigation with help electron backscatter diffraction (EBSD) to address it. The transition on the AA2198-AS is clear and results from the difference between small recrystallized grains in NZ and bent and elongated grains in TMAZ (Figure 5(e)). This sharp transition in the advancing side is due to the higher local shear coming from the opposite direction of the tool rotation and plate motion [34].

The effect of PWHT on the grain size of the nugget center can be seen in Figure 7. The grain size before applying heat treatment was around  $8\ \mu\text{m}$ . No considerable difference in grain size in the nugget center was found after PWHT. Significant grain growth in the nugget area was yet reported by using PWHT on Al-Cu-Li alloy [35], which is mainly attributed to the solution heat treatment at higher temperatures.

### 3.2. Micro-hardness maps

2D micro-hardness maps of the ND-CWD section of the joints were illustrated in Figure 8 for the as-welded samples (AW-T3 and AW-T8) and the post-weld heat-treated samples (PW-T8 and PSPW-T8). The loss of hardness properties was found in all the typical regions of as-welded samples. The minimum hardness values (around 85 HV) were observed in the S-shape zone, the TMAZ/HAZ of the advancing side, and the shoulder affected region (upper region within the NZ), as depicted in Figure 8(a,d). Furthermore, the comparison between AW-T3 and AW-T8 samples (Figure 8(a,d)) reveals that applying a heat treatment prior to welding could not improve the hardness in the joint area due to the significant effect of the subsequent welding process.

The sample fracture locations in tension are represented on the two-dimensional hardness maps with red lines in Figure 8. The as-welded samples (AS-T3 and AS-T8) failed at the TMAZ/HAZ of the advancing side (AA2198). The post-weld heat-treated tensile specimens failed at the TMAZ/HAZ on the retreating side (AA2024). The fracture locations correspond to minimal hardness regions for the different joint variants.

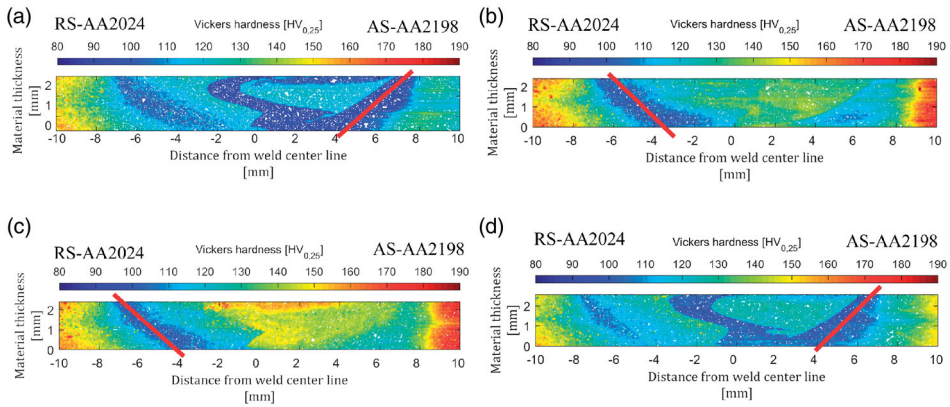


**Figure 8.** 2D micro-hardness map across the ND-CW plane for samples: (a) AW-T3, (b) PW-T8, (c) PSPW-T8, and (d) AW-T8. The solid lines depict location of fracture during monotonic tensile tests.

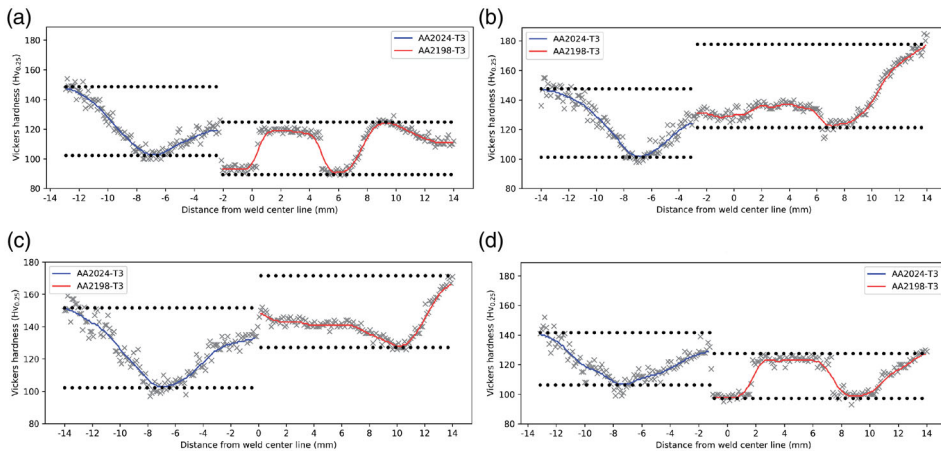


**Figure 9.** Micro-hardness distributions accomplished at mid-thickness of different joint variants: (a) AW-T3, (b) PW-T8, (c) PSPW-T8, and (d) AW-T8. Post-weld heat treatment enhanced the hardness properties on AA2198 side.

Micro-hardness profiles along the CWD are shown in [Figure 9](#) for all the joint variants. Regarding post-weld heat treatments, [Figure 9\(b\)](#) (PW-T8) and [Figure 9\(c\)](#) (PSPW-T8) show that applying an aging post-welding heat treatment on joints (compared to [Figure 9\(a\)](#)) significantly improved the hardness properties in the minimal hardness regions found in the as-welded samples. PW-T8 and PSPW-T8 samples consequently demonstrated higher and more homogeneous hardness properties. [Figure 9\(c\)](#) (PSPW-T8) shows that stretching the sample before aging treatment significantly improved the hardness on the advancing side and in the S-shape zone, that is, the regions with minimal hardness for as-welded joints. Stretching before aging of Al-Li alloys produces well-distributed intragranular dislocation structures. The dislocations perform as heterogeneous nucleation sites for the strengthening precipitates [36]. The improved hardness could be related to a higher precipitate density combined with lower precipitate sizes based on the Kampmann–Wagner numerical model [18].

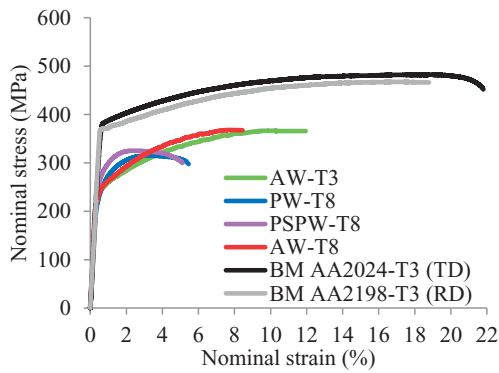


**Figure 10.** Mechanical properties of base metals (BM) and FSWed joints in as-welded and post-weld heat-treated conditions.

**Table 2.** Tensile characteristics of base metals (BM) and joint variants.

Sample code	YS (MPa)	UTS (MPa)	EI (%)
BM AA2024-T3 (TD)	380	482	22
BM AA2198-T3 (RD)	368	467	19
AW-T3	234	362	14
PW-T8	242	316	6
PSPW-T8	275	324	5
AW-T8	232	361	8

However, the post-welding treatments were shown to slightly impair the hardness properties in the TMAZ/HAZ regions on the retreating side (RS-AA2024) due to possible coarsening of precipitates in HAZ [18]. Additional microscopy analyses are presented in the following sections.

### 3.3. Mechanical testing for global characterizations

Mechanical properties of the base metals (BMs) and FSWed joints in as-welded and post-weld heat-treated conditions can be seen in Figure 10. The 0.2% offset yield strength (YS), ultimate tensile strength (UTS), and elongation (EI) are reported in Table 2. The mechanical performance of the base metals is quite similar to each other according to the tensile direction in reference to the rolled direction, that is, the transverse direction for AA2024 and the rolling direction for AA2198. These special material directions were purposely chosen to optimize the joint strength. Subsequently, applying the FSW process for manufacturing AW-T3 joint decreased the yield strength around 30% in comparison with base metals. In respect to recovering the mentioned loss of the joint mechanical properties, applying pre-weld heat treatment had no significant positive impact. Moreover, the joint elongation decreased around 4% (AW-T3 vs. AW-T8). Also, PW-T8 sample shows that applying post-weld heat treatment negligibly improved the yield strength compared to the as-welded samples. However, samples subjected to a combination of pre-stretching and post-welding heat treatment (PSPW-T8) exhibited the highest yield strengths, being about 18% stronger than the as-welded samples. It is worth mentioning that the pre-stretching step improves the strength of the as-weld joint (AW-T3) to around 262 MPa due to work hardening

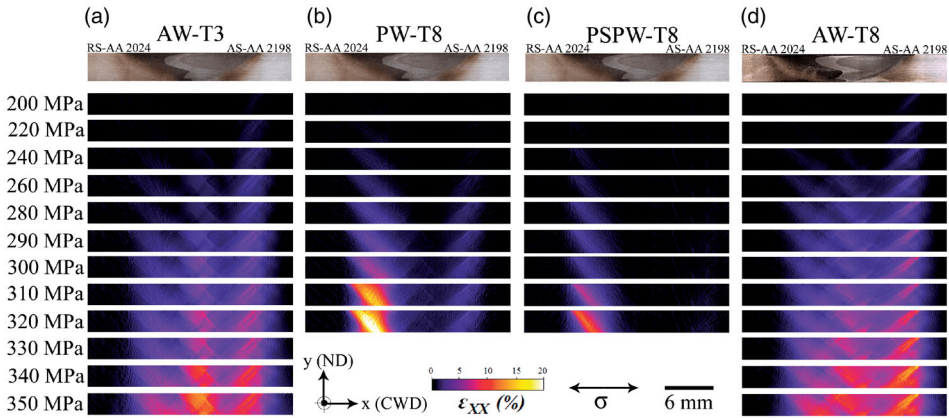


**Figure 11.** The local in-plane strain distribution map acquired by OHR-DIC for samples (a)AW-T3, (b)PW-T8, (c)PSPW-T8, and (d)AW-T8. The localization of strain for as-welded samples occurred at the sample middle and TMAZ/HAZ of AA2198 side. The post-weld heat treatment altered it to TMAZ/HAZ of AA2024 side.

based on Figure 10. Thus, improvement of the yield properties of PSPW-T8 is mainly attributed to work hardening rather than the applied heat treatment. In light of the fact that the current research deals with dissimilar joints, a local investigation of strain concentration within the joints is needed to understand better the effect of heat treatment on the joint mechanical performance.

### 3.4. Local mechanical characterization via digital image correlation technique

The local strain distribution maps of CWD-ND plane, acquired by DIC technique for all the joint variants, are depicted in Figure 11. Figure 11 confirms that the deformation within the joints is heterogeneous. However, as-welded samples and post-weld heat-treated samples behaved differently. Intense strain concentration regions are interestingly matched with regions experiencing the weakest micro-hardness properties in Figure 8. In addition, the location of the fracture is consistent with the lowest hardness areas and regions with the highest strain localization.

Average plastic strain vs. position along CWD at different stress levels is depicted in Figure 12. The strain localization first occurred in the TMAZ/HAZ on the advancing side of as-welded sample AW-T3, for macroscopic stresses as low as 200 MPa as shown in Figure 12(a). For higher stress levels (above 240 MPa), irreversible deformations are conjointly developed in the S-shape zone in the center of the weld and the TMAZ/HAZ on the AA2198 side with equivalent strain levels. However, for post-weld heat-treated samples (Figure 12(b,c)), no strain localization was observed in the S-shape zone in the center of the weld, regardless of the macroscopic loading condition. Furthermore, strain localization developed mainly in the TMAZ/HAZ on the retreating side (AA2024) instead of the advancing side. Besides, strain localization in the TMAZ/HAZ on the advancing side above 280 MPa was not found in PSPW-T8 samples than PW-T8 samples. Finally, based on Figure 11(d), the intensity of the strain localization

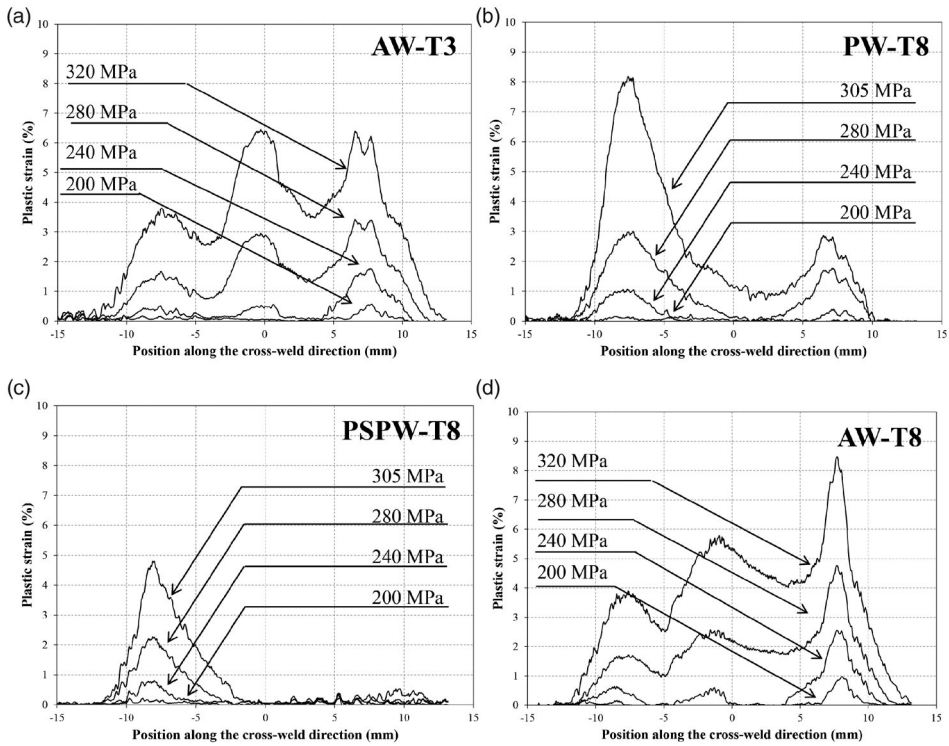


**Figure 12.** Average plastic strain vs. position along CWD at different stress levels. (a) AW-T3, (b) PW-T8, (c) PSPW-T8, and (d)AW-T8.

in the S-shape zone in the center of the weld was less pronounced for AW-T8 sample as compared to AW-T3 sample in equivalent macroscopic loading conditions.

To summarize, the combination of pre-stretching and post-welding heat treatment ultimately strengthened the responsible location for failure in as-welded samples. However, the joint heat treatment faces the following challenges: (1), AA2198 material naturally demonstrates a more pronounced response to age hardening in comparison with AA2024. (2), AA2198 experienced higher work hardening during stretching joint regions due to lower hardness in the as-welded condition. Thus; the challenges led to a higher chance for re-precipitation and strengthening in AA2198 side. Subsequent deformation within the joint after post-weld heat treatment was heterogeneous without improving the UTS and El of the joint, and only failure location changed from AA2198 to AA2024 side. Nevertheless, the YS improved, which is a more critical design parameter.

### 3.5. Fractographic analysis

The micrographs of the fracture surfaces of different joint variants can be seen in [Figure 13](#). The fracture surfaces of as-welded samples ([Figure 13\(a,d\)](#)) exhibited ductile features with no evidence of dimples related to TMAZ/HAZ of AA2198 material. In contrast, the ductile fracture surface of post-welding heat-treated samples located at the TMAZ/HAZ AA2024 and contained large dimples surrounded by small ones. The

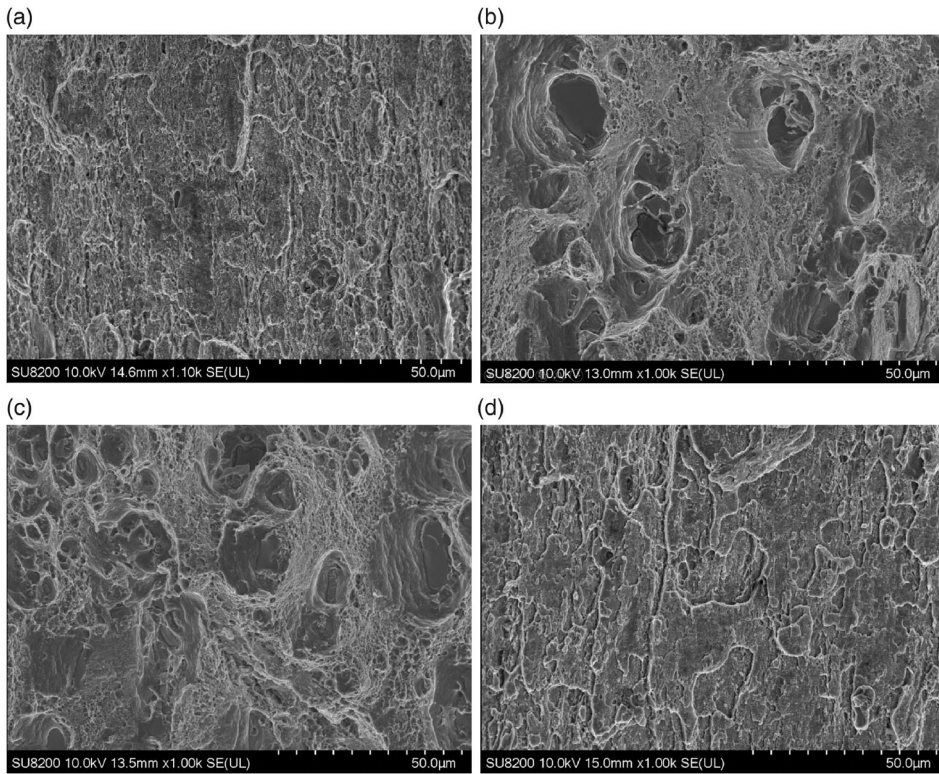


**Figure 13.** Micrographs of the fracture surfaces in TMAZ/HAZ of as-welded and post-weld heat treated samples observed by SEM in secondary electron mode after tensile tests: (a) AW-T3 (advancing side), (b) PW-T8 (retreating side), (c) PSPW-T8 (retreating side), and (d) AW-T8 (advancing side).

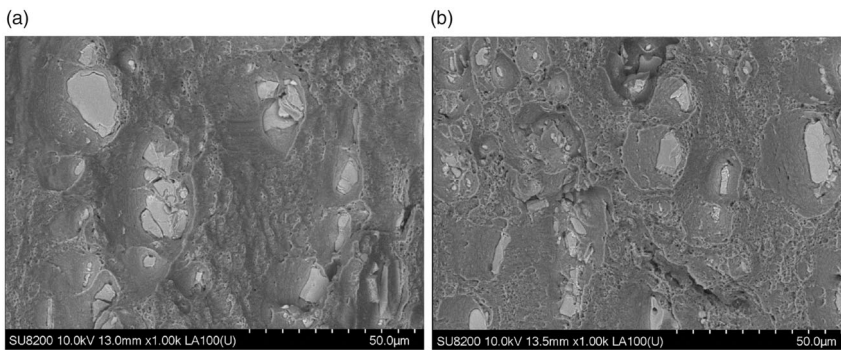


**Figure 14.** Micrographs of the fracture surfaces for heat treated samples observed by SEM in back-scattered electron mode after monotonic tensile tests: (a) PW-T8 and (b) PSPW-T8.

back-scattered electron micrographs in [Figure 14](#) from the TMAZ/HAZ AA2024 revealed that coarse and densely distributed intermetallic particles play a key role in forming large dimples and fracture processes. Based on our previous investigation on the base metal, these particles containing Fe and Si act as microvoid nucleation sites in ductile materials [24].

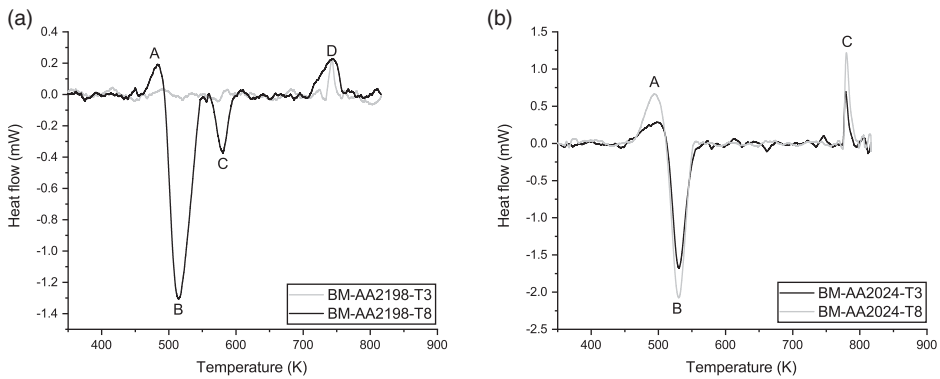


**Figure 15.** DSC results of base metal, (a) AA2198 and (b) AA2024.

### 3.6. DSC analyses and temperature measurements

DSC results of base metals AA2198 and AA2024 are reported in [Figure 15](#). It can be seen in the black curve of [Figure 15\(a\)](#), that the dissolution of GP-zones of AA2198 material occurred at the first endothermic peak A around 470 K [37]. The precipitation of T1 ( $\text{Al}_2\text{CuLi}$ ) occurs at peaks B [38]. The small peak C is related to precipitation of ( $\text{Al}_2\text{Cu}$ ) and peak D at high temperatures (750 K) shows the dissolution of the precipitates [39]. The effect of applying T8 heat treatment can be seen in the gray curve of [Figure 15\(a\)](#), where peaks A, B, and C disappeared. It confirms the complete reaction of T1 ( $\text{Al}_2\text{CuLi}$ ) and  $\theta$  ( $\text{Al}_2\text{Cu}$ ) precipitation as the main strengthening phase. The DSC result of AA2024 can be found in the black curve of [Figure 15\(b\)](#) and peaks A, B, and C are related to dissolution GP-zones, precipitation of S( $\text{Al}_2\text{CuMg}$ ) and precipitates dissolution, respectively [40]. Besides, comparing [Figure 15\(a,b\)](#) reveals that the precipitates dissolution temperature of AA2198 is lower than AA2024. In other words, AA2198 material is more prone to precipitate dissolution in high-temperature exposure than AA2024, resulting in lower hardness at TMAZ/HAZ of AA2198 in [Figure 8\(a\)](#) after the FSW process. In order to have a better idea about the temperature history during the FSW process, the temperature of sample AW-T3 in HAZ and TMAZ regions of AA2024 and AA2198 materials are reported in [Figure 16](#). Comparing the temperature measurements with the black curve of [Figure 15](#) conveys that the temperature during welding is high enough for both precipitates growth and partial dissolution in HAZ/TMAZ of both materials. Microscopy images of HAZ/TMAZ can provide more details about the precipitates present in HAZ/TMAZ, which covers the following section.

### 3.7. EDS analyses of the precipitation state

SEM images of precipitate evolution in TMAZ/HAZ of AA2024 and AA2198 before and after applying weld heat treatment can be seen in [Figure 17](#). Comparing [Figure 17\(a,b\)](#) clearly shows that using post-weld heat treatment resulted in the reprecipitation in the advancing side (AA2198 material). In order to have more details, higher magnification of rectangular A in [Figure 17\(a\)](#) with EDS maps is reported in [Figure 18](#). Based on phase morphology, EDS maps, and Rioja and Liu [11], it can be concluded that the

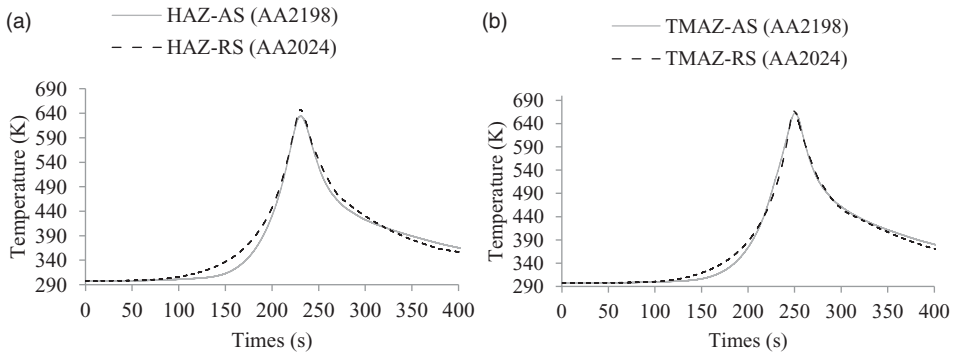


**Figure 16.** Temperature measurement during FSW process of AW-T3 sample; (a) HAZ and (b) TMAZ.

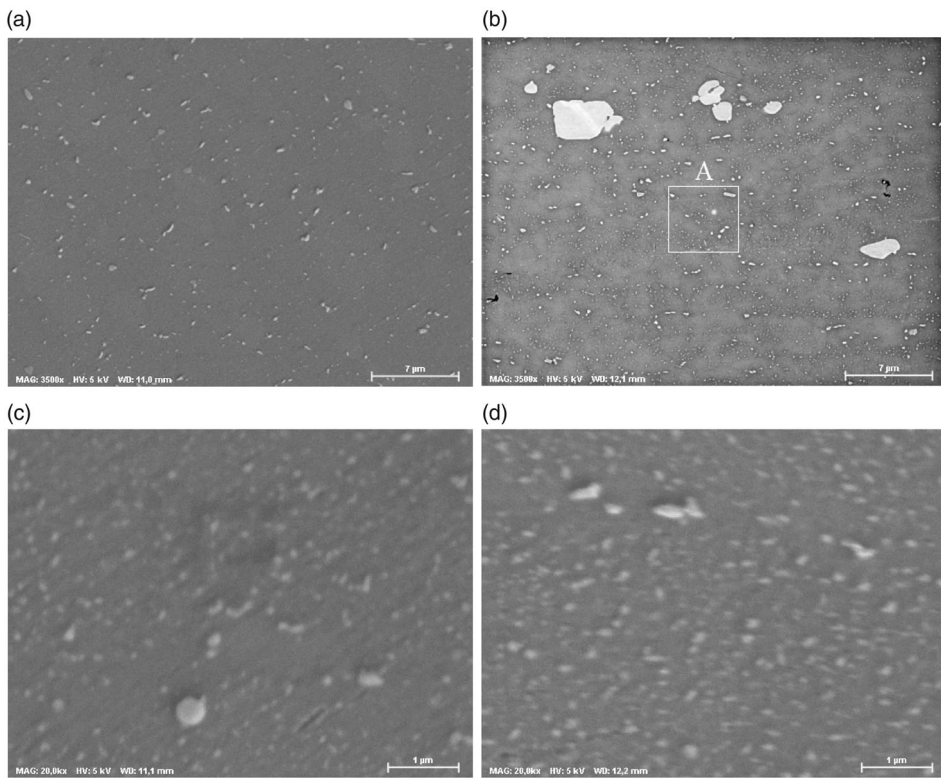


**Figure 17.** SEM images of precipitate evolution in TMAZ/HAZ as a result of PWHT, (a) advancing side of sample AW-T3, (b) advancing side of sample PSPW-T8, (c) retreating side of sample AW-T3, and (d) retreating side of sample PSPW-T8.

new precipitates are T1 ( $\text{Al}_2\text{CuLi}$ ) and  $\theta$  ( $\text{Al}_2\text{Cu}$ ); which is in agreement with the DSC result in Figure 15(a). On the other hand, the comparison between Figure 17(c,d) reveals that post-weld heat treatment has no significant effect on HAZ/TMAZ of AA2024.

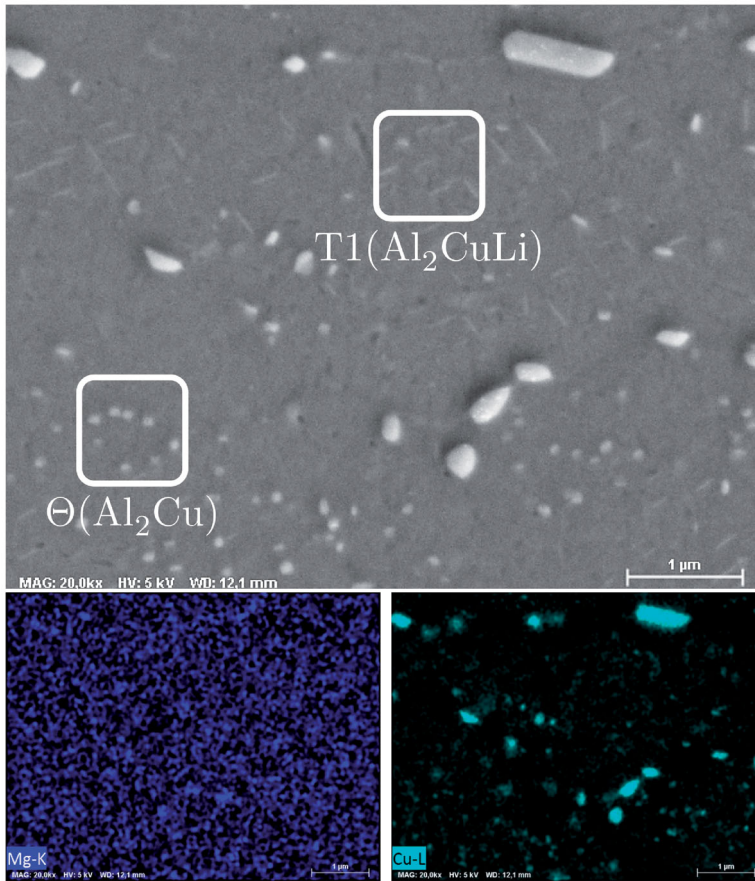


**Figure 18.** SEM and EDS maps of rectangular A in Figure 17(b) with higher magnification. Re-precipitation of T1 ( $\text{Al}_2\text{CuLi}$ ) and  $\theta$  ( $\text{Al}_2\text{Cu}$ ) is clear.

#### 4. Conclusions

The mechanical performances of dissimilar AA2024/AA2198 FSWed joints were examined in both T3 and T8 pre-weld and post-weld heat treatment conditions. Post-welding heat treatments, with and without a pre-stretching operation, were applied on an as-welded structure in T3 conditions to document the evolution of the joint mechanical properties. The intricate relationship between heat treatments, the local precipitation states in the different regions on the joint, and the local mechanical behavior (micro-hardness characterization and *in-situ* tensile testing paired with DIC techniques) within the different regions of the joints (NZ, TMAZ, HAZ) were investigated. The conclusions are as follows:

- AA2198 and AA2024 materials with T3/T8 heat treatment provide joints with comparable mechanical properties due to the subsequent impairing effect of the welding process. Thus, T3 heat treatment versus T8 is cost-effective.

- The TMAZ/HAZ on the AA2198 side was responsible for joint failure in the as-welded condition, identified with the DIC technique and the micro-hardness characterization. Post-weld heat treatments successfully strengthened this region and slightly improved the yield properties of the joints compared to as-welded joints. However, it was not effective in terms of improving global mechanical properties due to intense strain localization located AA2024 side.
- Improving the mechanical properties of the AA2024–AA2198 joint by pre-stretching and heat treatment is a challenge due to receiving inhomogeneous work hardening during stretching and a different response of AA2024 and AA2198 materials to heat treatment.

## Acknowledgments

We would like to express our appreciation to Ludovic Diez-Jahier, Remi Bertrand, Hossein Monajati, Eric Marcoux, and Michel Orsini for their help during this research. Without their valuable assistance, this work would not have been completed.

## Disclosure statement

No potential conflict of interest was reported by the author(s).

## Funding

A part of the research presented in this paper was financed by the Fonds de Recherche du Québec-Nature et Technologies through the Aluminum Research Centre-REGAL.

## References

- [1] Kumar Rajak D, Pagar DD, Menezes PL, et al. Friction-based welding processes: friction welding and friction stir welding. *J Adhes Sci Technol*. 2020;34(24):2613–2625.
- [2] Li C, Zhang D, Gao X, et al. Numerical simulation and experimental research on friction stir welding of 2024-T3 aeronautical aluminum alloy. *J Adhes Sci Technol*. 2021; (0):1-19
- [3] Mardalizadeh M, Khandaei M, Safarkhanian MA. Influence of travel speed on the microstructural evaluation and mechanical characteristics of bobbin tool friction stir welded thick AA5456-h112 plates. *J Adhes Sci Technol*. 2021;35(1):90–20.
- [4] Li X, Li C, Liang Z, et al. Research on the corrosion behavior of double-side friction stir welded 6082al alloy thick plate. *J Adhes Sci Technol*. 2020; (0):1–13.
- [5] Gopkalo O, Liu X, Long F, et al. Non-isothermal thermal cycle process model for predicting post-weld hardness in friction stir welding of dissimilar age-hardenable aluminum alloys. *Mater Sci Eng: A*. 2019;754:205–215.
- [6] Kumar PV, Reddy GM, Rao KS. Microstructure, mechanical and corrosion behavior of high strength AA7075 aluminum alloy friction stir welds-effect of post weld heat treatment. *Defense Technol*. 2015;11(4):362–369.
- [7] Baghdadi AH, Rajabi A, Selamat NFM, et al. Effect of post-weld heat treatment on the mechanical behavior and dislocation density of friction stir welded Al6061. *Mater Sci Eng: A*. 2019;754:728–734.
- [8] Kumar KA, Murigendrappa S, Kumar H. A bottom-up optimization approach for friction stir welding parameters of dissimilar AA2024-T351 and AA7075-T651 alloys. *J Mater Eng Perform*. 2017;26(7):3347–3367.

- [9] Park SW, Yoon TJ, Kang CY. Effects of the shoulder diameter and weld pitch on the tensile shear load in friction stir welding of AA6111/AA5023 aluminum alloys. *J Mater Proc Technol.* 2017;241:112–119.
- [10] Heidarzadeh A, Mironov S, Kaibyshev R, et al. Friction stir welding/processing of metals and alloys: a comprehensive review on microstructural evolution. *Prog Mater Sci.* 2021;117:100752.
- [11] Rioja RJ, Liu J. The evolution of Al-Li base products for aerospace and space applications. *Metall Mater Trans A.* 2012;43(9):3325–3337.
- [12] Cavaliere P, Cabibbo M, Panella F, et al. 2198 Al-Li plates joined by friction stir welding: mechanical and microstructural behavior. *Mater Des.* 2009;30(9):3622–3631.
- [13] Bucior M, Kluz R, Kubit A, et al. Analysis of the possibilities of improving the selected properties surface layer of butt joints made using the FSW method. *Adv Sci Technol Res J.* 2020;14(1):1–9.
- [14] Bitondo C, Prisco U, Squilace A, et al. Friction-stir welding of AA 2198 butt joints: mechanical characterization of the process and of the welds through doe analysis. *Int J Adv Manuf Technol.* 2011;53(5–8):505–516.
- [15] Ma YE, Xia Z, Jiang R, et al. Effect of welding parameters on mechanical and fatigue properties of friction stir welded 2198 t8 aluminum-lithium alloy joints. *Eng Fract Mech.* 2013;114:1–11.
- [16] Wang B, Chen F, Liu F, et al. Enhanced mechanical properties of friction stir welded 5083al-h19 joints with additional water cooling. *J Mater Sci Technol.* 2017;33(9):1009–1014.
- [17] Sharma V, Sharma C, Upadhyay V, et al. Enhancing mechanical properties of friction stir welded joints of Al-Si-Mg alloy through post weld heat treatments. *Mater Today: Proc.* 2017;4(2):628–636.
- [18] Zhang Z, Wan Z, Lindgren LE, et al. The simulation of precipitation evolutions and mechanical properties in friction stir welding with post-weld heat treatments. *J Mater Eng Perform.* 2017;26(12):5731–5740.
- [19] Dewan MW, Wahab MA, Sharmin K. Effects of post weld heat treatments (PWHT) on friction stir welded AA2219-T87 joints. Paper presented at the 12th International Manufacturing Science and Engineering Conference collocated with the JSME/ASME 2017 6th International Conference on Materials and Processing; 2017 June 4–8; Los Angeles, CA.
- [20] Chu G, Sun L, Lin C, et al. Effect of local post weld heat treatment on tensile properties in friction stir welded 2219-O al alloy. *J Mater Eng Perform.* 2017;26(11):5425–5431.
- [21] Moradi MM, Aval HJ, Jamaati R. Effect of pre and post welding heat treatment in sic-fortified dissimilar AA6061-AA2024 FSW butt joint. *J Manufact Proc.* 2017;30:97–105.
- [22] Cerri E, Leo P. Mechanical properties evolution during post-welding-heat treatments of double-lap friction stir welded joints. *Mater Des.* 2011;32(6):3465–3475.
- [23] Zhang J, Feng X, Gao J, et al. Effects of welding parameters and post-heat treatment on mechanical properties of friction stir welded AA2195-t8 Al-Li alloy. *J Mater Sci Technol.* 2018;34(1):219–227.
- [24] Robe H, Zedan Y, Chen J, et al. Microstructural and mechanical characterization of a dissimilar friction stir welded butt joint made of AA2024-T3 and AA2198-T3. *Mater Characteriz.* 2015;110:242–251.
- [25] Texier D, Zedan Y, Amoros T, et al. Near-surface mechanical heterogeneities in a dissimilar aluminum alloys friction stir welded joint. *Mater Des.* 2016;108:217–229.
- [26] Masoumi M, Zedan Y, Texier D, et al. The influence of tool geometry on mechanical properties of friction stir welded AA-2024 and AA-2198 joints. Saint-Colomban (Canada): The International Committee for Study of Bauxite, Alumina & Aluminium (ICSOBA); 2016.
- [27] Khalilabad MM, Zedan Y, Texier D, et al. Effect of tool geometry and welding speed on mechanical properties of dissimilar AA2198-AA2024 FSWed joint. *J Manufact Proc.* 2018;34:86–95.

- [28] Zhu C, Lv K, Chen B. On the s-phase precipitates in 2024 aluminum alloy: an atomic-scale investigation using high-angle annular dark-field scanning transmission electron microscopy. *J Mater Res.* 2020;35:1582–1589.
- [29] Lv K, Zhu C, Zheng J, et al. Precipitation of T1 phase in 2198 Al–Li alloy studied by atomic-resolution HAADF-STEM. *J Mater Res.* 2019;34(20):3535–3544.
- [30] Chandler H. Heat treater's guide: practices and procedures for nonferrous alloys. Materials Park (OH): ASM International; 1996.
- [31] Zhang Sf, Zeng Wd, Yang Wh, et al. Ageing response of a Al–Cu–Li 2198 alloy. *Mater Des.* 2014;63:368–374.
- [32] Bridier F, Stinville JC, Vanderesse N, et al. Microscopic strain and crystal rotation measurement within metallurgical grains. In: *Key engineering materials*. Vol. 592. Trans Tech Publ;Switzerland ;2014. p. 493–496.
- [33] Zhang C, Huang G, Cao Y, et al. Microstructure and mechanical properties of dissimilar friction stir welded AA2024-7075 joints: influence of joining material direction. *Mater Sci Eng: A.* 2019;766:138368.
- [34] Cho JH, Boyce DE, Dawson PR. Modeling strain hardening and texture evolution in friction stir welding of stainless steel. *Mater Sci Eng: A.* 2005;398(1–2):146–163.
- [35] Lin Y, Lu C, Wei C, et al. Influences of friction stir welding and post-weld heat treatment on Al–Cu–Li alloy. *Adv Eng Mater.* 2018;20(2):1700652.
- [36] Rodgers B, Prangnell P. Quantification of the influence of increased pre-stretching on microstructure-strength relationships in the Al–Cu–Li alloy AA2195. *Acta Materialia.* 2016;108:55–67.
- [37] Ringer S, Muddle B, Polmear I. Effects of cold work on precipitation in Al–Cu–Mg–(Ag) and Al–Cu–Li–(Mg–Ag) alloys. *Metallurg Mater Transact A.* 1995;26(7):1659–1671.
- [38] Dorin T, Deschamps A, De Geuser F, et al. Quantification and modeling of the microstructure/strength relationship by tailoring the morphological parameters of the T1 phase in an Al–Cu–Li alloy. *Acta Materialia.* 2014;75:134–146.
- [39] Dorin T, Deschamps A, De Geuser F, et al. Quantitative description of the T1 formation kinetics in an Al–Cu–Li alloy using differential scanning calorimetry, small-angle x-ray scattering and transmission electron microscopy. *Phil Magaz.* 2014;94(10): 1012–1030.
- [40] Genevois C, Deschamps A, Denquin A, et al. Quantitative investigation of precipitation and mechanical behavior for AA2024 friction stir welds. *Acta Materialia.* 2005;53(8): 2447–2458.